Nuclear Instruments and Methods in Physics Research B 104 (1995) 212–221

ELSEVIER

NIM B
Beam Interactions
with Materials & Atoms

Applications of ion-beam tomographic element microanalysis (ITEM)

R.M.S. Schofield[1]

Physics Department, University of Oregon, Eugene, OR 97403, USA

Abstract

Developments in tomographic analysis using PIXE are reviewed. Simulated 2D and tomographic analyses show that for a variety of specimens about 20 times more data counts are required for tomographic than for 2D analysis. When shape information available from noise-free STIM tomography is incorporated, this factor is reduced to about 4. Three applications for which ITEM is preferable to 2D analysis are demonstrated. First, ITEM of an ant mandible embedded in amber, a specimen that would be destroyed by sectioning, reveals that zinc is still present and localized. Second, the Ca content of the distal portion of a fruitfly Malpighian tubule is measured with ITEM to be 170 ng. This measurement could not be made using techniques that require sectioning. Finally, ITEM is used to avoid contamination from sectioning in an analysis of Ca in the retina of a fruitfly.

1. Introduction

Greater sample penetration is a distinct advantage of nuclear microscopy over competing electron microprobe techniques. Thicker specimens can be analyzed using nuclear microscopy with either two-dimensional (2D) or tomographic techniques [1]. For 2D PIXE, X-ray attenuation and ion energy loss in the specimen decrease the accuracy of the measurements, but limits on the possible error due to these effects can be calculated from STIM measurements at two different angles [1]. Tomographic techniques afford the possibility of accommodating these effects directly instead of as sources of uncertainty and also provide local rather than depth-averaged information. Tomographic sets of PIXE data do not normally contain the information necessary to account for X-ray attenuation and ion energy loss because PIXE data is not usually available for all elements in the specimen. The necessary supplemental information can be supplied directly through a fore-knowledge of the specimen, by using STIM tomography in conjunction with PIXE tomography or through other methods. Because this supplemental information is essential, tomographic analysis using PIXE is not referred to here as PIXE tomography but as Ion-beam Tomographic Element Microanalysis (ITEM).

This article will first briefly review developments in ITEM and then, using simulations, investigate the relative numbers of data counts needed for tomographic and 2D analysis. This will provide a partial answer to the question of how sensitive tomographic analysis is in comparison to 2D analysis. Results will then be presented demonstrating three different applications for which ITEM may be the preferred analytic technique.

2. Review

Reconstructions of element density in specimens heterogeneous in three dimensions were first presented in 1992 by the Eugene group [2]. STIM tomography was used in conjunction with PIXE tomography so that X-ray attenuation and variations in X-ray production cross section could be accounted for. Donner library software [3] for single photon emission tomography that iteratively corrects for photon attenuation was modified to accommodate ion energy loss as an effective attenuation of X-rays. The local X-ray production cross sections and the X-ray attenuation factors were calculated from the STIM density reconstruction. For this calculation, the element composition of the specimen was assumed to be homogeneous. Recently, Antolak and Bench [4] have developed software, also based on the Donner algorithms, that avoids this assumption of homogeneity by iteratively incorporating information from the element density reconstructions into the calculation of X-ray

[1]Also at: Department of Nuclear Physics, Lund University, Lund, Sweden.

SSDI 0168-583X(95)00386-X

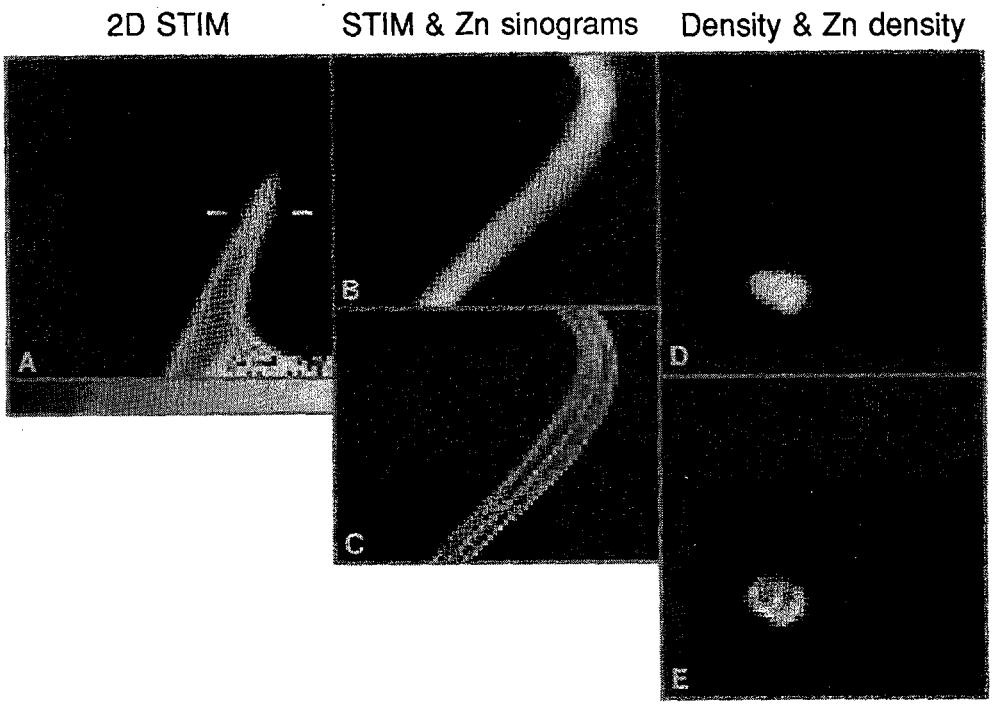

Fig. 1. ITEM of a lateral tarsal claw from a leg of a scorpion, *Pandinus sp.* (A) The 2D STIM image produced from energy-loss data for 2.7 MeV protons. The axis of rotation for tomography is vertical and near the center of the image. (B) The 50 line STIM tomographic data set (sinogram): the specimen was scanned along the 64-pixel line, indicated in the 2D image, at each of 50 angular orientations spaced evenly over 180°. Before reconstruction, projected (areal) densities were calculated from the energy loss data. (C) Sinogram of PIXE data for Zn. Data accumulation took about 15 min; the beam current was about 2 nA. (D) The density distribution for the claw section indicated in the 2D image. This 64×64 pixel density reconstruction was used to calculate the local X-ray production cross sections and attenuation factors needed to reconstruct the Zn distribution from the tomographic PIXE data. (E) The distribution of Zn. This distribution is consistent with the 3 bright lines visible in the PIXE sinogram. Frame edge: 400 μm (except for vertical edges of sinograms).

attenuation factors, production cross sections and areal densities. The algorithm was tested with a standard consisting of Ni and Cu–Be wires and with two simulated specimens. With successive hierarchical iterations, values converged on the correct element concentration for both the real and the simulated specimens, though it has not been shown that the correct element densities will be approached in all cases. Antolak and Bench also demonstrated an application of ITEM by analyzing a direct drive inertial confinement fusion target.

The Eugene and Livermore algorithms were compared using data for a scorpion sting. On the Eugene Sun Sparc station a 64×64 pixel reconstruction of a sting slice took 10 min using the Eugene software and 13 h using the Livermore software. Reconstruction using the Livermore software is time consuming because very many stopping power calculations are required for inhomogeneous specimens. Peak Zn concentrations of 25% as compared to 24% and Mn concentrations of 4.6% as compared to 3.8% were obtained using, respectively, the Livermore and the Eugene software packages.

In addition to the programs at Eugene and Livermore, an ITEM program has been initiated at Lund and a reconstruction of Lund microprobe data is used in Fig. 1 to illustrate ITEM. Although the group at Melbourne has not presented tomographic reconstructions, they have been developing methods of handling and displaying the large quantities of data needed for complete 3-dimensional analyses of specimens [5,6].

The group in Singapore has recently extended their work on PIXE depth profiling [7] and introduced an algorithm for ITEM that uses prior knowledge of the major element distribution instead of information from STIM tomography [8]. The iterative maximum-likelihood algorithm has been successfully tested on simulated data showing that as few as four views are needed for surprisingly accurate reconstructions.

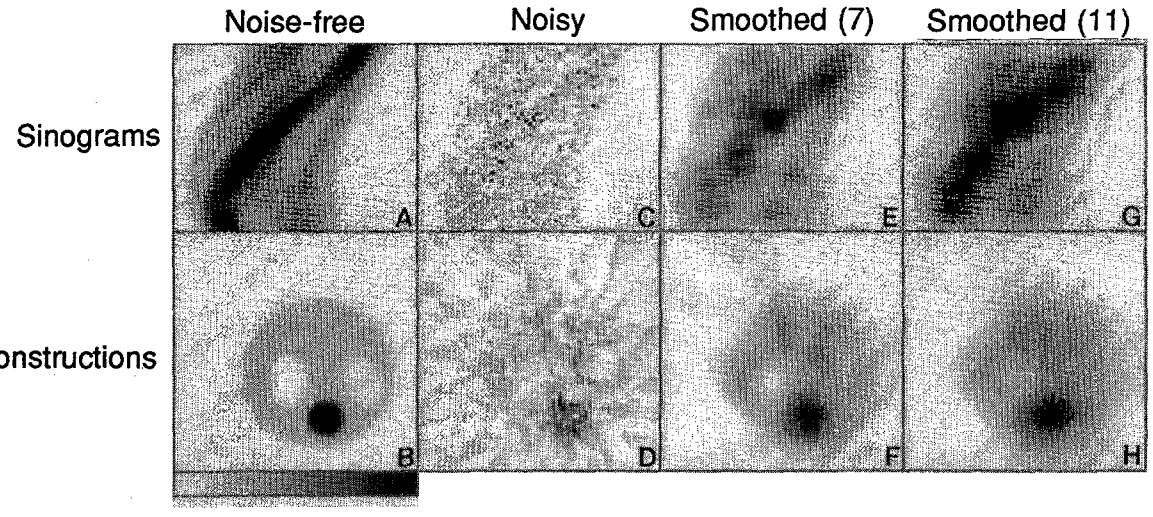

Fig. 2. Smoothing noisy sinograms to improve reconstructions. (A) The noise-free simulated data. (B) The reconstruction of the simulated specimen from this simulated data. (C) The simulated data with noise introduced to mimic data averaging 0.5 counts per data pixel. (D) The corresponding reconstruction. (E) The noisy sinogram smoothed using a smoothing width of 7 pixels. (F) The corresponding reconstruction. (G) The noisy sinogram after 11-pixel smoothing. (H) The corresponding reconstruction. Reconstruction (F) had the lowest n.m.d. from the reconstruction using noise-free simulated data (B).

3. Smoothing tomographic data to improve reconstructions

Considerable statistical fluctuations are often present in PIXE data because specimen damage or time considerations limit the permissible sample exposure. Statistical fluctuations in tomographic data sets result in artifacts in the reconstructions. Noisy data sets can be spatially smoothed to reduce statistical fluctuations and the resulting artifacts. Of course smoothing of the data set degrades the resolution of the reconstruction. There is, therefore, a balance to be attained between inaccuracies in the reconstruction associated with noise artifacts, and the inaccuracy of degraded resolution associated with data smoothing. The optimum width of the smoothing function for a particular proportion of statistical noise was investigated using simulated data sets. First simulated data were generated using the Donner phantom generation algorithms [3] and poisson noise introduced to mimic fluctuations from counting statistics. Several reconstructions were then computed using several different spatial smoothing widths for the noisy simulated data. These reconstructions from smoothed noisy "data" were each compared for accuracy to the reconstruction from the noise-free "data" using the normalized mean deviation (n.m.d.), determined as follows:

$$\text{n.m.d.} = \frac{\sum_{\text{pixels}} |P_{\text{clean}} - P_{\text{noisy}}|}{\sum_{\text{pixels}} P_{\text{clean}}},$$

where P_{clean} refers to a pixel value in a reconstruction from noise-free simulated data and P_{noisy} refers to the value of the corresponding pixel in the reconstruction from noisy simulated data. Mean instead of standard deviations were used so as not to over-emphasize large deviations. The smoothing width associated with the lowest n.m.d. was taken to be optimal.

The effects of smoothing the noisy "data" are illustrated in Fig. 2; simulated sinograms (tomographic data sets) are shown in the top row and the corresponding reconstructions in the bottom row. The smoothing width for the sinogram in column 3 was 7. The counts at each pixel were divided evenly among the 7^2 pixels centered at that pixel location. The n.m.d. for the reconstruction from this sinogram was the lowest in a series using smoothing widths of 1, 3, 5, 7, 9, 11, and 13.

Six simulated data sets for four simulated specimens were prepared. The simulated specimens are illustrated in Fig. 3 with reconstructions from several of the simulated data sets. From each of the six noise-free simulated data sets, 7 sets were prepared with differing proportions of noise. Table 1 shows the optimal smoothing width for each of these noisy simulated data sets. The four simulated specimens were designed to represent a range of specimen complexity. Even so, the optimal smoothing widths for each simulated data set vary little. This suggests that the optimal smoothing widths in this table should have general application to a range of real specimens and data sets. To test the dependance of the optimal smoothing width on the reconstruction algorithm, the reconstructions for simulated specimen B were

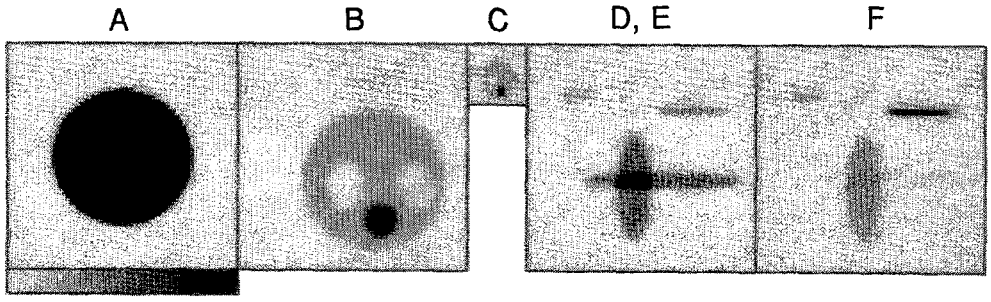

Fig. 3. Reconstructions of the 6 noise-free simulated data sets showing the four simulated specimens. These reconstructions do not reproduce the simulated specimens exactly, because the angle resolution and data pixel size for the simulated data were finite. Simulated specimen A, for example, was homogeneous. For reconstructions A, B, and D, 64 pixel lines for 50 views spaced evenly over 180° were simulated. For C, 16 pixel lines at 25 angles were generated for the same simulated specimen reproduced by reconstruction B. Simulated data for E and F consisted of 64 pixel lines at 100 angles. Although there were twice as many angular orientations in data set D as in E, the reconstructions were virtually identical and so only one is shown.

Table 1
Optimal smoothing widths. Each entry gives the smoothing width, number of iterations of the Donner Grady algorithm, and the n.m.d. for the reconstruction with the lowest n.m.d. selected from 28 reconstructions using 7 smoothing widths (1, 3, 5, 7, 9, 11, 13) for each of 4 variations in the number of iterations (usually 5, 10, 15, and 20). Reconstructions of the simulated data sets are shown in Fig. 3.

Average counts per data pixel[a]	Simulated data set					
	A	B	C	D	E	F
0.2	13, 5, 0.37	9, 10, 0.52	5, 2, 0.67	7, 10, 0.77	7, 10, 0.77	5, 10, 0.80
0.5	9, 5, 0.33	7, 10, 0.43	5, 2, 0.59	5, 10, 0.57	5, 10, 0.57	3, 10, 0.66
1	7, 5, 0.27	7, 10, 0.38	3, 2, 0.53	5, 10, 0.52	3, 10, 0.51	3, 10, 0.57
2	7, 10, 0.29	5, 10, 0.32	3, 10, 0.44	3, 10, 0.46	3, 10, 0.46	3, 10, 0.47
5	5, 10, 0.21	5, 15, 0.27	3, 15, 0.37	3, 10, 0.37	3, 20, 0.37	3, 20, 0.38
10	5, 10, 0.18	3, 10, 0.23	3, 15, 0.33	3, 20, 0.31	3, 20, 0.31	3, 10, 0.32
20	5, 15, 0.16	3, 15, 0.19	1, 5, 0.27	3, 20, 0.26	3, 20, 0.26	1, 20, 0.27

[a]A "data pixel" is a pixel bin that could contain counts: a pixel that has a non-zero value in the noise-free sinogram.

repeated using the Donner conjugate gradient algorithm, the algorithm used in the Livermore software [4]. Although the optimal number of iterations differed, the optimal smoothing width remained the same in each case.

4. Relative numbers of data counts needed for simulated 2D and tomographic analyses

Suppose that a slice of an unsectioned specimen was first analyzed using tomography, and then, for comparison, the specimen was physically sectioned and the slice analyzed using 2D PIXE. For the same accuracy, would the tomographic analysis require that the slice be exposed to more beam charge than the 2D PIXE analysis? This question was investigated using the simulated tomography data discussed above and simulated 2D data. The simulated 2D data were prepared by degrading the reconstructions shown in Fig. 3 with poisson noise. Since the tomographic "data" were smoothed, the 2D "data" were also smoothed using a range of smoothing widths (1, 3, 5, 7, 9 and 13). The optimally smoothed 2D "data" were then compared to the tomographic reconstructions of Table 1 again using the n.m.d.

This comparison of tomographic and 2D methods is demonstrated in the first two columns of Fig. 4. In the first column, at the top, is a simulated 2D data set consisting of a total of 381 data counts for the simulated specimen B shown in Fig. 3. Below it is the optimally smoothed (lowest n.m.d.) version of this 2D "data" set, having the lowest n.m.d. (0.30) with the noise-free version. The second column shows the simulated data set, consisting of 4345 counts, that was used to produce the optimal reconstruction in Table 1 that most nearly matched the 2D "data" set in accuracy (n.m.d. = 0.32). Thus for com-

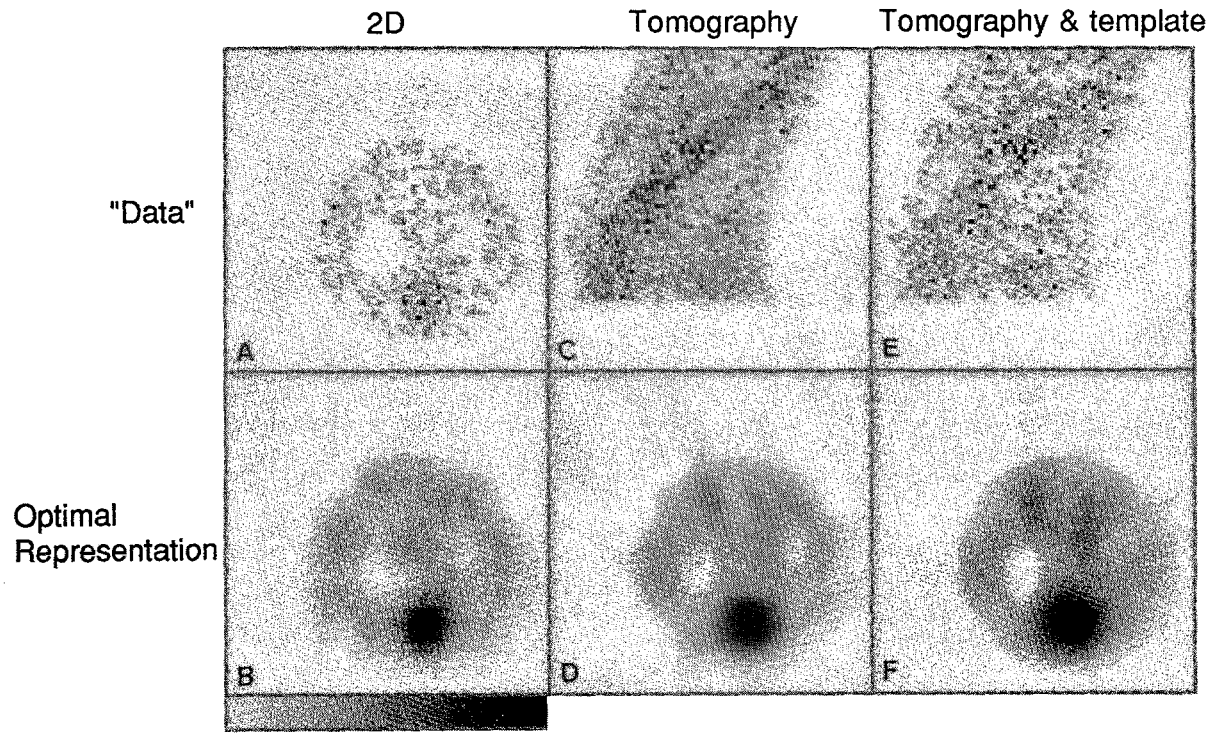

Fig. 4. The relative quantities of data counts needed for a 2D and a tomographic simulated analyses. All of the representations of the simulated specimen shown on the bottom row are similarly accurate, the top row shows the simulated data sets used for each of these representations. (A) A 2D set with 381 counts; (B) the optimally smoothed (smoothing width of 7) 2D "data" set. (C) Tomographic "data" set with 4345 counts. (D) The corresponding optimal reconstruction (5-pixel sinogram smoothing). (E) Tomographic "data" set consisting of 995 counts. (F) The corresponding optimal reconstruction (7-pixel sinogram smoothing), using the template scheme to incorporate shape information from the noise-free reconstruction. About 10 times as many data counts were required for tomographic as opposed to 2D "analysis" in this case. When shape information was incorporated this factor was reduced to about 2.5.

parable accuracy, the tomographic "data" set required about 10 times more data counts than were contained in the 2D data set.

Is it possible to decrease the number of counts required for tomography and thus the exposure time needed for PIXE tomography by incorporating information from STIM tomography? The STIM tomography data used to correct PIXE tomography data for ion energy loss and X-ray attenuation is free from counting statistics so the resulting density reconstructions are more accurate than the noisy element density reconstructions from PIXE data. Two methods of incorporating information from the STIM reconstruction were investigated. The first method involved modifying the reconstruction algorithm so that the reconstruction from noisy data (PIXE) was confined to regions where values in the noise-free (STIM) reconstruction exceeded some threshold. The reconstruction algorithm was not modified for the second method. Instead, the portion of the "noisy" reconstruction in regions below some density threshold in the "noise-free" reconstruction was simply discarded. This method was termed the template method and was the more successful method in all cases investigated.

The template method is demonstrated in the last column of Fig. 4. The simulated data set at the top of the column, consisting of 995 counts, was smoothed and the simulated specimen reconstructed. Then the reconstruction from noise-free simulated data (representing the STIM density reconstruction and shown in Fig. 3B) was used as a template: pixels in the reconstruction of noisy "data" were set to zero if they corresponded to pixels in the noise free reconstruction that fell below some threshold value. The result, shown at the bottom of column 3 is about as accurate as the reconstruction next to it, at the bottom of column 2. Thus the template scheme reduced the required data counts by, in this case, a factor of about 4.

Table 2 summarizes the comparison of simulated 2D and tomographic analyses. An entry of 10 in the table indicates that for comparable accuracy ten times as much data was required for tomographic "analysis" then was needed for 2D "analysis".

Table 2
The ratio of tomographic to 2D data counts for comparable accuracy. Bold numbers are for reconstructions that incorporate shape information using the template scheme

Tomographic data average counts per data pixel[a]	Simulated data set[b]				
	A	B	C	D	F
0.1	**1**				
0.2	**1**	**2**			**2**
0.5	**1**,5	**2.5**	5	**2.5**	**2.5**
1	**1**,5	10	**2**,5		
2	4	10	**1**,4		**2**
5	5	**10**	5	**10**,25	**2.5**,25
10	5	**5**,20	**2**,5	**10**	**2**,20
20	4	20	**4**	**4**,40	20
50		**2.5**,25			
100		20			
200		**4**,20			
500		25			

[a]A "data pixel" is a pixel bin that could contain counts: a pixel that has a non-zero value in the noise-free sinogram.
[b]The simulated specimens are shown in Fig. 3.

The count ratios were the highest for high resolution "data" of complex simulated specimens (sets B, D, and F). For these simulated analyses an average of 20 times as many data counts were required for tomographic analysis than for 2D analysis. When specimen shape information was incorporated using the template scheme, this factor was reduced to about 4.

5. Applications: An unsectionable specimen

Tomographic element microanalysis promises to be useful for specimens that would be damaged by sectioning or exposure to vacuum. The fossilized biological inclusions in amber are such specimens. The degree to which the original chemical composition of the entombed animals is preserved is of interest [9]. Many arthropods are endowed with large quantities of heavy metals in the jaws. The degree to which these accumulations have diffused away may serve as an indicator of the state of preservation of the entombed animals.

Fig. 5 illustrates ITEM of a piece of Pliocene Tanzanian "amber" bearing a fossil ant (about 3 million years old). Four MeV protons were used for this and the other analyses reported below. The amber was shaved to within a fraction of a millimeter of the enclosed ant mandibles (4 MeV protons travel through about 1/4 mm of amber) and tomographic STIM and PIXE data sets for three slices were collected as previously described [2] at 100 angles spaced evenly over 180 degrees. Even though the Zn density image (Fig. 5c) is blurred due to poor X-ray statistics, it is evident that the Zn is still localized and has not diffused throughout the amber. The Zn density and total density reconstructions can be used to obtain the Zn concentration. In this section it reaches about 0.2%. This concentration is an order of magnitude below the peak concentrations found in modern ant mandibles. The concentration may be low partly because the Zn density reconstruction is blurred, but it is unlikely that blurring could account for an order of magnitude. It is possible that the majority of the Zn leached completely out of the amber, that this species accumulates less Zn, or that the highest concentrations are found in a part of the mandible not analyzed.

6. A measurement of total Ca content

Techniques that require sectioning cannot be used to measure the total quantity of an element in a microscopic structure. Such measurements have been shown to be useful and have been accomplished using 2D PIXE [1]. ITEM affords the possibility of more accurate mass measurements. This element specific "nano-balance" application of ITEM is demonstrated here with a measurement of the calcium content of the distal portion of the Malpighian tubules (similar to kidneys) of a fruitfly (*Drosophila melanogaster*).

The distal portion of the Malpighian tubule was dissected and placed on a fragment of 0.5 μm thick silicon nitride foil [10]. The fragment of foil was glued to a small wire attached to the stepping motor shaft. The foil supported itself and the portion of organ and was small enough to fit completely into the 640 μm region scanned for each of the reconstructed sections, as required by the reconstruction algorithm.

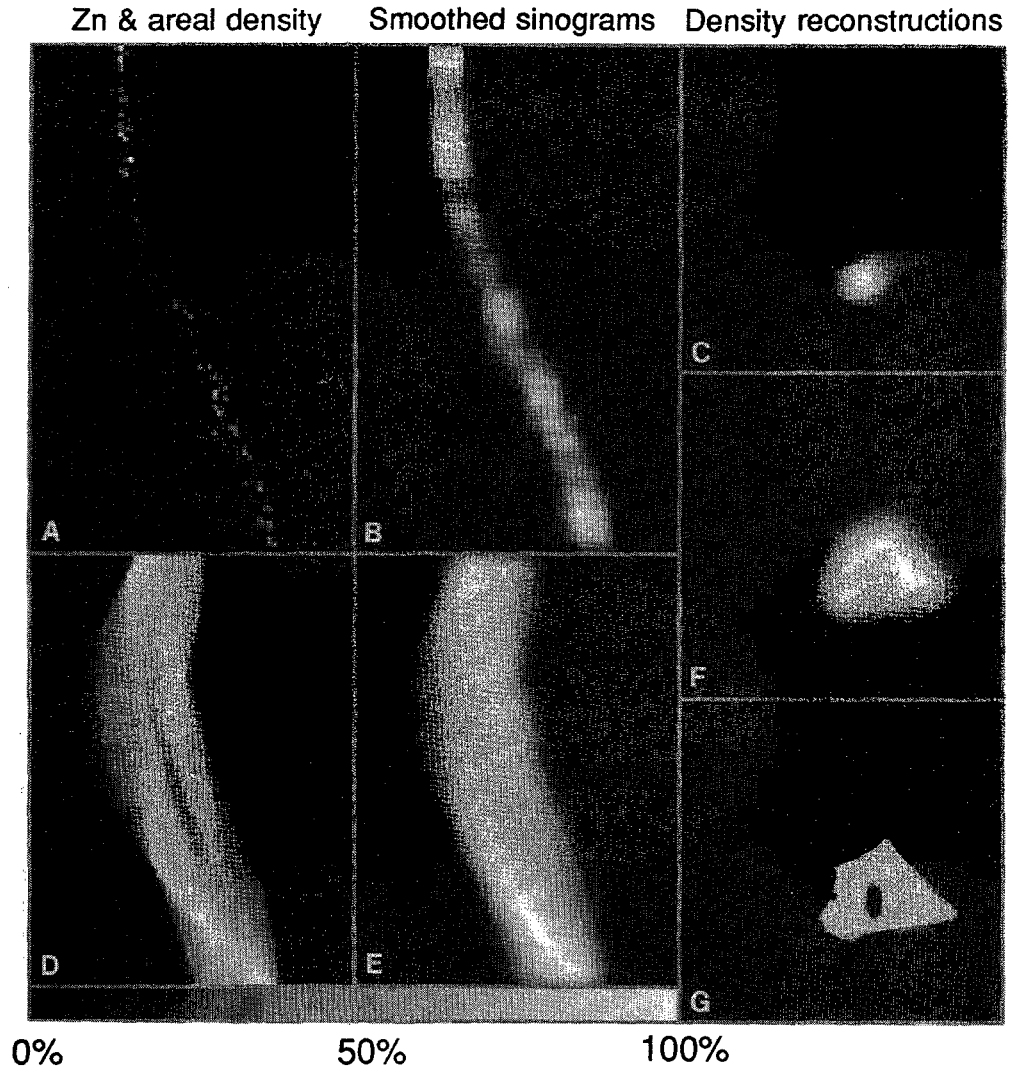

Fig. 5. ITEM of 3 million year old amber containing an ant mandible, showing that mandibular zinc is still present and localized. (A) Zn PIXE data: 64 pixel lines at 100 angular orientations over 180°. (B) PIXE data smoothed according to Table 1 with a width of 7. (C) Reconstruction of the Zn density distribution. (D) Areal density sinogram derived from STIM data: 256 pixel lines at 100 angular orientations. The pixels are not square for convenience of display. (E) Areal density sinogram smoothed to match the resolution of the smoothed Zn PIXE data. (F) Reconstruction of density from the smoothed areal density sinogram. This reconstruction matches the resolution of the Zn density reconstruction and was used for calculating X-ray production cross sections, attenuation factors and Zn concentrations. (G) Reconstruction of the unsmoothed areal density sinogram showing the hollow in the amber that was occupied by the mandible; remaining tissue surrounds this cavity and is apparently about the same density as the amber. White (maximum values): (A) 2 counts; (B) 0.7 counts; (C) 0.0016 gm/cm^2; (D) 0.022 gm/cm^2; (E) 0.020 gm/cm^2; (F) 1.1 gm/cm^3; (G) 1.2 gm/cm^3. Frame edges: 0.5 mm (except vertical edges of sinograms).

Fig. 6 shows data and reconstructions for 10 contiguous sections covering the distal portion of one tubule. The total Ca content in these ten sections was 170 ng. The Livermore software was used for these reconstructions so that the matrix would be iteratively corrected for high concentrations of Ca (about 25%). All of the 20×20 pixel sections were reconstructed in about 100 min. Data accumulation took about an hour. The variation in X-ray production cross section in this specimen was about 20%; the maximum attenuation of Ca X-rays was also about 20%.

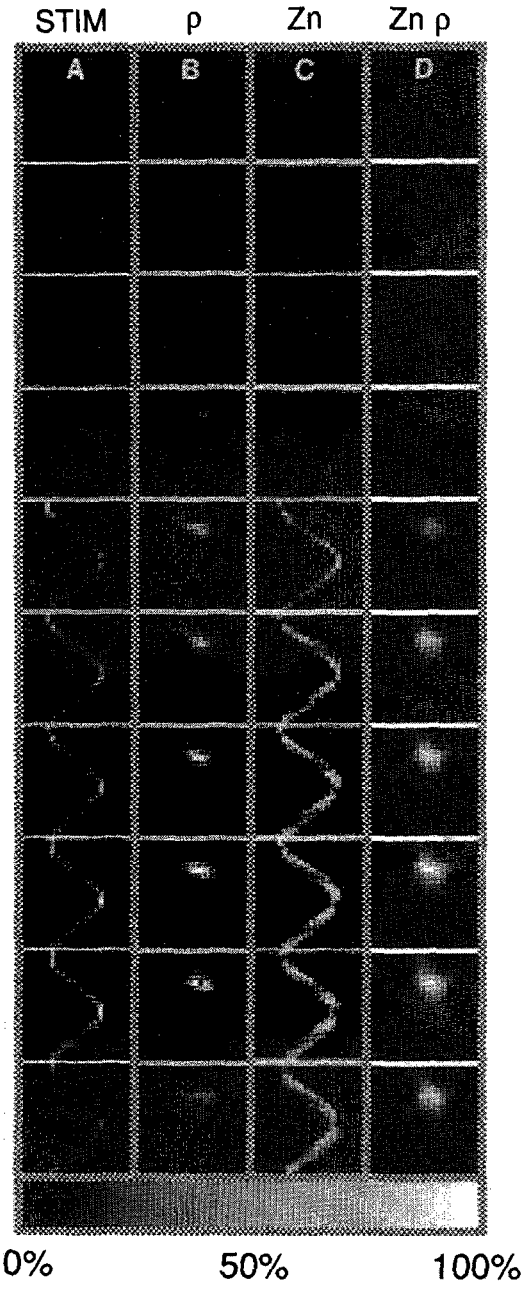

Fig. 6. ITEM measurement of the total Ca content in the most distal portion of the Malpighian tubule of a fruitfly, a measurement that could not be made using techniques that require sectioning. The first column shows 10 areal density sinograms from STIM for the 10 contiguous slices of the specimen. The second column shows the density reconstructions, the third shows the Ca PIXE data sinograms and the fourth shows the Ca density reconstructions. The tomographic data consists of 20 pixel lines at 25 angular orientations of the specimen. This portion of the Malpighian tubules contains 170 ng of Ca. White: (A) 0.014 gm/cm^2; (B) 0.25 gm/cm^3; (C) 174 counts; (D) 0.02 gms/cm^3. Frame edges: 0.64 mm (except vertical edges of sinograms).

7. Avoidance of contamination

The eyes of fruitflies (*Drosophila melanogaster*) have been extensively investigated because they are suitable models for developmental genetics [11]. Examinations of whole fruitfly heads using 2D PIXE have revealed elevated concentrations of Ca in the eyes [12]. Calcium is hypothesized to be an internal transmitter in the phototransduction process [13] and so the location of the Ca accumulations within the eye is of interest. It is not clear from 2D PIXE images of whole heads whether the Ca is spread evenly throughout the retina and optic lobes of the brain or whether the Ca is localized in a particular region. Two-dimensional PIXE of a sectioned retina would reveal localizations but Ca contamination during sample preparation confused a 2D analysis of a similar specimen, a bee brain [14]. To avoid contamination introduced during sectioning, a fly head was analyzed tomographically. Fig. 7 shows the results of this analysis. The sinograms were not smoothed (Table 1 would suggest a smoothing width of 3), preserving resolution at the expense of overall accuracy. At the right hand side of the second row is the reconstruction of Ca density. The outer 1/3 of the retina appears to stand out in Ca density. This Ca enriched region may occupy even less than the outer 1/3 of the retina as it is only a pixel or two in thickness in the image, and thus at the limit of resolution. For concentration measurements the sinogram was smoothed, so the resolution was even poorer and the value must be considered a lower limit for the Ca enriched region. The Ca concentration in the outer half of the retina averaged 0.4% of dry mass and in the inner half, 0.2%. The potassium distribution is shown for comparison with the Ca distribution. The K concentration was fairly uniform in the retina, averaging 0.9%. In the brain it averaged 1.3%.

Phototransduction takes place in the rhabdomeres, situated in the proximal 3/4 of the retina and not in the distal (outer) extreme. Thus it seems unlikely that the distal Ca accumulation is directly associated with the rhabdomeres and phototransduction. It seems more likely that the elevated Ca concentrations are associated with structures or cells that occupy only the distal portion of the retina, such as the primary pigment cells, cone cells, pseudocones or corneas [15].

During the $1\frac{1}{2}$ hours of tomographic PIXE data collection, the scanned regions were exposed to about 2.4×10^{16} 4 MeV protons per cm^2. This exposure was required because the geometric efficiency of the detector was only 0.00021. STIM before and after PIXE tomography showed that beam damage was not confined to the 3 tomographic slices (only 1 is shown in Fig. 7). Mass losses averaged about 8% in the scanned regions and about 2% in regions of the head that were not scanned. The migration of energy

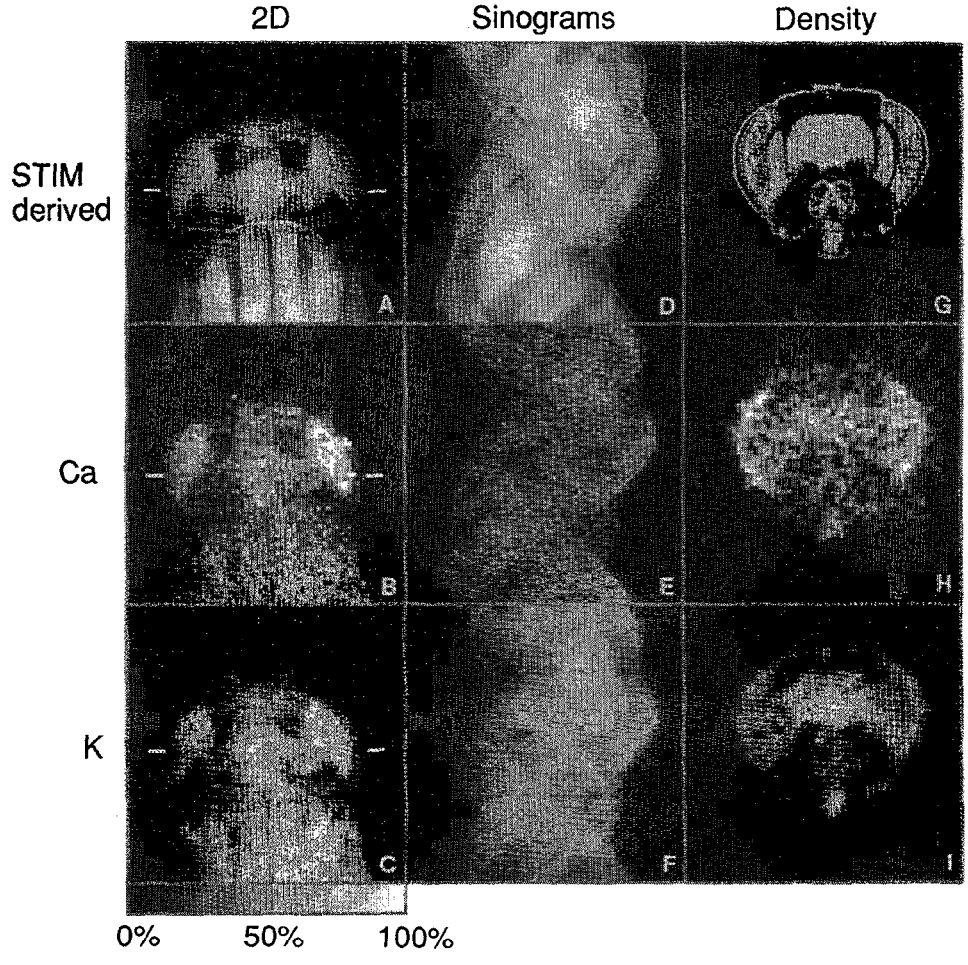

Fig. 7. ITEM reveals an elevated Ca density in the distal (outer) portion of a fruitfly's retinas. (A) A 2D image, derived from STIM, showing the head and part of the thorax of the fruit fly. The retinas occupy most of the left and right side of the head. (B), (C) 2D PIXE images in Ca and potassium X-rays respectively. The X-ray detector is on the right, so X-rays from the left side are more attenuated. (D), (E) and (F) Sinograms for the slice indicated by white lines in the 2D images, showing the STIM derived areal density, Ca X-ray counts, and potassium X-ray counts respectively. The 200 horizontal lines (256 pixels wide for STIM, 64 for PIXE) are for projections spread evenly over 360°. For display convenience, sinogram pixels are not square. (G) The tomographic reconstruction of the density distribution. The thick outer symmetric structures on the left and right are sections of the retinas. Proximal (inward) to each of the retina sections, and separated by low density gap, the section cuts through the lamina and proximal to it and separated by another low density gap, the optic lobe and the rest of the brain [11, 13, 15]. (H) The Ca density distribution for the tomographic section showing an elevated calcium content in the distal portion of the retinas. (I) The potassium distribution, included for comparison. White: (A) 0.023 gm/cm^2; (B) $\geq$ 35 counts; (C) 107 counts; (D) 0.025 gm/cm^2; (E) 38 counts; (F) 22 counts; (G) 0.68 gm/cm^3; (H) $\geq$ 0.0030 gm/cm^3; (I) 0.016 gm/cm^3. Frame edges: 1 mm (except vertical edges of sinograms).

from the isolated scan regions probably contributed to the success of the analysis because previous studies of similar specimens [16, 12] suggest that the mass losses would have been prohibitively large if the entire head and not just isolated regions had been subjected to this exposure.

8. Conclusions

In practice, ITEM is probably somewhat less sensitive than 2D analysis because tomography requires about an order of magnitude more data counts. However, ITEM may become a preferred alternative for specimens that

cannot be easily sectioned, specimens that cannot be exposed to vacuum, and for investigations of specimen contamination. In addition to these applications, ITEM is a unique tool for measuring element content in microscopic structures.

Acknowledgements

Part of this work was supported by the Dept. of Nuclear Physics, Lund University. Harlan Lefevre, University of Oregon, offered many helpful suggestions, made the Eugene microprobe available and provided for its maintenance. Travel funds were provided by the Department of Physics, University of Oregon.

References

[1] R.M.S. Schofield and H.W. Lefevre, Nucl. Instr. and Meth. B 77 (1993) 217.
[2] R.M.S. Schofield and H.W. Lefevre, Nucl. Instr. and Meth. B 72 (1992) 104.
[3] R.H. Huesman, G.T. Gullberg, W.L. Greenberg and T.F. Budinger, Users Manual: Donner Algorithms for Reconstruction Tomography, Publication 214, Lawrence Berkeley Laboratory Technical Information Department, Berkeley, 1977.
[4] A.J. Antolak and G.S. Bench, Nucl. Instr. and Meth. B 88 (1994) 297.
[5] A. Saint, G. Bench, G. Moloney and G.J.F. Legge, Proc. 7th Aust. Conf. on Nuclear techniques of Analysis, Melbourne, 1991, p. 209.
[6] A. Saint, M. Cholewa and G.J.F. Legge, Nucl. Instr. and Meth. B 75 (1993) 504.
[7] S.C. Liew, K.K. Loh and S.M. Tang, Nucl. Instr. and Meth. B 85 (1994) 621.
[8] S.C. Liew, I. Orlic and S.M. Tang, these Proceedings (ICNMTA'94) Nucl. Instr. and Meth. B 104 (1995) 222.
[9] G.O. Poinar, Life in Amber (Stanford University Press, Stanford, Ca, 1992).
[10] H.W. Lefevre, R.M.S. Schofield and D.R. Ciarlo, Nucl. Instr. and Meth. B 54 (1991) 47.
[11] B. Dickson and E. Hafen, in: The Development of *Drosophila melanogaster*, eds. M. Bate and A.M. Arias (Cold Spring Harbor Laboratory Press, Plainview, New York, 1993) p. 1327.
[12] H.W. Lefevre, R.M.S. Schofield, J.C. Overley and J.D. MacDonald, Scanning Microscopy 1 (1987) 879.
[13] W.L. Pak, S.R. Grabowski, in: The Genetics and Biology of Drosophila, Vol. 2a, eds. M. Ashburner and T.R.F. Wright (Academic Press, London, 1980) p. 553.
[14] F. Watt and G.W. Grime, Nucl. Instr. and Meth. B 30 (1988) 356.
[15] D.R. Kankel et al., in: The Genetics and Biology of Drosophila, Vol. 2d, eds. M. Ashburner and T.R.F. Wright (Academic Press, London, 1980) p. 312.
[16] G.S. Bench, H.W. Lefevre and G.J.F. Legge, Nucl. Instr. and Meth. B 88 (1994) 229.